

# Study of the Ar metastable atom population in a hollow cathode discharge by means of a hybrid model and spectrometric measurements

N. Bagner<sup>a)</sup> and A. Bogaerts

*Department of Chemistry, University of Antwerp (UA), Universiteitsplein 1, B-2610 Wilrijk-Antwerp, Belgium*

Z. Donko

*Research Institute for Solid State Physics and Optics, Hungarian Academy of Sciences, P.O. Box 49, H-1525, Budapest, Hungary*

R. Gijbels

*Department of Chemistry, University of Antwerp (UA), Universiteitsplein 1, B-2610 Wilrijk-Antwerp, Belgium*

N. Sadeghi

*Laboratoire de Spectrometrie Physique [Unité Mixte de Recherche (UMR) 5588], Université Joseph Fourier-Grenoble and Centre National de la Recherche Scientifique (CNRS), BP 87, 38402, St. Martin d'Herès, France*

(Received 26 August 2004; accepted 14 April 2005; published online 22 June 2005)

The role of the metastable Ar atoms in a 1-cm-diameter cylindrical hollow cathode discharge (HCD) is studied self-consistently based on a hybrid model and experimental measurements in the pressure range of 0.3–1 Torr and currents of 1–10 mA. The model comprises submodels based on the principles of Monte Carlo and fluid simulations. The Monte Carlo model describes the movement of the fast electrons, fast Ar and Cu atoms, and fast Ar<sup>+</sup> and Cu<sup>+</sup> ions as particles, while in the fluid model, the slow electrons, Ar<sup>+</sup>, Cu<sup>+</sup> ions, Cu, and Ar metastable atoms are treated as a continuum. The population of the two metastable states within the 3p<sup>5</sup>4s configuration (<sup>3</sup>P<sub>2</sub> and <sup>3</sup>P<sub>0</sub>) were combined into one collective level, for which the continuity equation was written. Typical calculation results are, among others, the two-dimensional profiles of the production and the loss rates of Ar metastable atoms, as well as the metastable atom densities and fluxes throughout the complete HCD. Moreover, the calculated radial profiles (averaged over the axial direction) of the Ar metastable atom density are compared with experimental radial density profiles recorded by laser absorption spectroscopy. The relative importance of the different processes determining the Ar metastable population is analyzed, as well as the influence of pressure and voltage on them. Experimental results evidence the presence of the metastable atom production source at the cathode surface, probably originating from fast Ar<sup>+</sup> ions and Ar atoms impinging on it. Comparison between experimental and calculated Ar metastable atom densities shows a good agreement at low pressures, but at 1 Torr the calculated values differ by a factor of 2 from the measured ones. Several possible explanations for this discrepancy are discussed. © 2005 American Institute of Physics.

[DOI: 10.1063/1.1929857]

## I. INTRODUCTION

Hollow cathode discharges (HCDs) are being used in a wide variety of application fields, such as in plasma processing (ion etching, thin-film deposition, and surface treatment),<sup>1</sup> in lasers,<sup>2–4</sup> and in spectroscopic analysis.<sup>5–9</sup> To improve the results in these application fields, it is important to understand the different mechanisms involved in the discharge. This can be achieved by numerical modeling. In previous works,<sup>10,11</sup> we have concentrated on the study of the properties of HCDs and on the charged particles present in the plasma. In the present work, we will focus on the behavior of the Ar metastable atoms (Ar<sup>m</sup>) and their interaction with the other particles present in the HCD.

The general processes, which determine the metastable

atom density in glow discharges, were studied by Ebbinghaus.<sup>12</sup> Since then many papers have been published, where the Ar<sup>m</sup> metastables are being studied either experimentally (using atomic absorption spectroscopy,<sup>13–16</sup> plasma-induced emission spectroscopy,<sup>17</sup> laser-induced fluorescence,<sup>18</sup> etc.) as well as by numerical models (where the transport of metastable atoms is described by continuity equations, yielding the metastable density).<sup>19–21</sup> The population of Ar<sup>m</sup> metastable atoms was studied, experimentally and with the use of balance equations, in various kinds of plasmas including afterglow,<sup>22,23</sup> dc,<sup>24</sup> rf,<sup>25–27</sup> and helicon<sup>15</sup> discharges. Also some studies have been performed with respect to the role of metastables in the glow discharge with formation of a positive column (PC).<sup>28,29</sup>

In the present paper, we will analyse the role of Ar<sup>m</sup> metastable atoms in a HCD, using a metastable transport model, which is combined with a hybrid Monte Carlo fluid

<sup>a)</sup>Electronic mail: neyda.bagner@ua.ac.be

model for electrons,  $\text{Ar}^+$  and  $\text{Cu}^+$  ions, fast Ar atoms ( $\text{Ar}^f$ ), and fast and thermal Cu atoms. A similar combination of models has been applied in the literature for the simulation of glow discharges with planar cathode, both in dc,<sup>30</sup> and rf (Ref. 26) regimes. The advantage of this procedure is that it allows following the influence of the metastable atoms on the electron energy distribution, the ionization rates, the ion and electron densities, etc., as well as the influence of these parameters on the metastable atom density. Moreover,  $\text{Ar}^m$  metastables play a decisive role in the ionization of the sputtered Cu atoms.

Calculated metastable atom density profiles (axially averaged) are compared with experimental density profiles measured by laser absorption in similar discharge geometry (1-cm diameter, 3 cm long) and at the same conditions (0.3–1 Torr pressure and 1–10-mA current).

## II. DESCRIPTION OF THE MODEL

### A. Assumptions of the model

The discharge gas was assumed to be argon at room temperature and uniformly distributed throughout the discharge, i.e., the thermal motion of the gas atoms is neglected. The other species considered in the model are fast and slow electrons, singly charged fast and slow positive argon ( $\text{Ar}^+$ ) and copper ( $\text{Cu}^+$ ) ions, metastable  $\text{Ar}^m$  atoms, fast Ar atoms, and fast and slow Cu atoms. As fast particles are considered the particles for which it is necessary to get the energy distribution in order to accurately calculate the (inelastic or elastic) collision and/or sputtering rates.

The  $\text{Ar}^f$  atoms are formed by elastic collisions of  $\text{Ar}^+$  ions and  $\text{Cu}^+$  ions with the background Ar gas and are assumed to have energies higher than 1 eV. The fact that we consider a fraction of the Ar atoms as fast particles does not contradict the assumption that the gas is uniformly distributed throughout the discharge, because the fast  $\text{Ar}^f$  atom density is much lower (four orders of magnitude) than the density of the discharge gas.<sup>11</sup> Nevertheless, these fast  $\text{Ar}^f$  atoms can be important in the discharge because they play a role in ionization and excitation of Ar atoms and in the cathode sputtering (see below).

The fast Cu atoms ( $\text{Cu}^f$ ) are the sputtered atoms from the cathode. Indeed the Cu atoms are emitted with an initial energy of several eV and they are considered as fast particles until they are thermalized, i.e., mainly due to elastic collisions with the background gas.

The fast  $\text{Ar}^+$  and fast  $\text{Cu}^+$  ions are considered in the cathode dark space (CDS), where these ions gain energy from the electric field and they are described through a Monte Carlo approach.

The electrons are split up into two groups:<sup>31</sup> the fast electrons, with high enough energy to cause inelastic collisions, and the slow electrons, which do not have enough energy. The energy threshold for considering electrons as fast particles was 4.6 eV, which corresponds to the ionization energy of the Ar metastable levels.

The two metastable levels of Ar,  $^3P_2$  and  $^3P_0$ , which are lying at 11.55 and 11.72 eV above the ground state, respectively, have been combined into one collective level, lying at

11.55 eV.<sup>30</sup> This assumption was made based on the fact that according to their statistical weights,  $g=2J+1$ , where  $J$  is the total angular momentum of the state, the  $^3P_0$  level is expected to be five times less populated than the  $^3P_2$  level and in our experiments, density ratios close to 1/7 were measured in the HCD. This significantly lower population of the  $^3P_0$  level was also confirmed in previous studies in different kinds of discharges.<sup>13,32</sup> Besides that, our interest in studying the metastable  $\text{Ar}^m$  atoms is concerned with their influence on the electrical properties of the discharge, on the secondary electron emission, and on the ionization of the sputtered Cu atoms, for which only the total metastable density is important.

In the following, we will emphasize on the description of the  $\text{Ar}^m$  metastable fluid model because of the comparison between calculated and experimental results. The models applied for the electrons,  $\text{Ar}^+$  ions, and fast  $\text{Ar}^f$  atoms were mainly explained in our previous papers.<sup>10,11</sup> Here they will be described only briefly, pointing out the modifications done in order to account for processes which were not considered in Refs. 10 and 11. In order to analyze the loss of  $\text{Ar}^m$  metastable atoms by ionization with the sputtered Cu atoms, it is also necessary to know the Cu atom density. Therefore, we had to incorporate in the model three submodels: a Monte Carlo (MC) model for the fast  $\text{Cu}^f$  atoms, a MC model for the fast  $\text{Cu}^+$  ions, and a fluid model for the slow Cu atoms and  $\text{Cu}^+$  ions. These models are described in a forthcoming paper, related specifically to the study of the sputtered atoms and the corresponding ions,<sup>33</sup> but the main outline of these models, for a dc glow discharge and for a HCD, is given in Refs. 34 and 35, respectively.

### B. Fluid models

The fluid model considers the plasma as a continuum, which is characterized by macroscopic, ensemble-averaged magnitudes. The transport of this continuum is described by solving, for each kind of plasma species (electrons, positive and negative ions, metastable atoms, etc.), some moments of the collisional Boltzmann equations: the continuity, the momentum, the energy equations, etc. In a fluid model for collision-dominated plasma, it is assumed that the velocity distribution of each fluid is in hydrodynamic equilibrium with the local electric field.<sup>36</sup> In that case the momentum balance equation is replaced by the drift-diffusion approximation and the energy equation is simplified by the local-field approximation. Hence, the transport of each fluid can be described by the continuity and flux equations only.<sup>37</sup> In the case of charged fluids, it is necessary to couple these equations with the Poisson's equation in order to calculate the electric field. As fluid we consider here: the slow electrons in the negative glow (NG) (i.e., the slow electrons are present only in the NG, because in the CDS they always gain energy from the electric field), as well as the  $\text{Ar}^+$  ions, the  $\text{Cu}^+$  ions, the thermalized Cu atoms, and the  $\text{Ar}^m$  metastable atoms, in the complete discharge.

TABLE I. Production and loss processes considered in the fluid model for the  $\text{Ar}^m$  metastable atoms.

Production processes		Rates or rates coefficients
$\text{Ar} + e_f \rightarrow \text{Ar}^m + e_f$	Electron-impact excitation	$S_{\text{exc},e}$ [calculated in MC- $e$ ] <sup>a</sup>
$\text{Ar} + \text{Ar}^+ \rightarrow \text{Ar}^m + \text{Ar}^+$	Ion-impact excitation	$S_{\text{exc},\text{Ar}^+}$ [calculated in MC- $\text{Ar}^+$ ] <sup>b</sup>
$\text{Ar} + \text{Ar}^f \rightarrow \text{Ar}^m + \text{Ar}^f$	Atom-impact excitation	$S_{\text{exc},\text{Ar}^f}$ [calculated in MC- $\text{Ar}^f$ ] <sup>b</sup>
$\text{Ar}^+ + e \rightarrow \text{Ar}^m + h\nu$	Radiative recombination	$k_{\text{rec}} = 1 \times 10^{-11} \text{ cm}^3 \text{ s}^{-1\text{c}}$
Loss processes		
$\text{Ar}^m + e_f \rightarrow \text{Ar}^+ + 2e_f$	Electron-impact ionization	$S_{e,\text{ion},m}$ [calculated in MC- $e$ ] <sup>d</sup>
$\text{Ar}^m + \text{Ar}^m \rightarrow \text{Ar}^+ + \text{Ar} + e_f$	Pooling ionization	$k_{\text{met}} = 6.4 \times 10^{-10} \text{ cm}^3 \text{ s}^{-1\text{e}}$
$\text{Ar}^m + e \rightarrow \text{Ar}^* + e \rightarrow \text{Ar} + h\nu + e$	Effective-electron quenching	$k_q = 1 \times 10^{-8} \text{ cm}^3 \text{ s}^{-1\text{e}}$
$\text{Ar}^m + \text{Cu} \rightarrow \text{Ar} + \text{Cu}^+ + e$	Penning ionization	$k_{\text{Pen}} = 2.6 \times 10^{-10} \text{ cm}^3 \text{ s}^{-1\text{f}}$
$\text{Ar}^m + \text{Ar} \rightarrow \text{Ar} + \text{Ar}$	Two-body collision	$k_{2B} = 2.3 \times 10^{-15} \text{ cm}^3 \text{ s}^{-1\text{g}}$
$\text{Ar}^m + 2\text{Ar} \rightarrow \text{Ar}_2^* + \text{Ar}$	Three-body collision	$k_{3B} = 1.4 \times 10^{-34} \text{ cm}^6 \text{ s}^{-1\text{g}}$
Diffusion to the walls, followed by deexcitation at the walls		$D_{\text{Ar}^m} = 54 \text{ cm}^2 \text{ s}^{-1\text{h}}$

<sup>a</sup>Taken from Refs. 38–40.<sup>b</sup>Taken from Ref. 41.<sup>c</sup>Taken from Ref. 42.<sup>d</sup>Taken from Ref. 43.<sup>e</sup>Taken from Ref. 29.<sup>f</sup>Taken from Ref. 30.<sup>g</sup>Taken from Ref. 13.<sup>h</sup>Taken from Ref. 23.

### 1. Fluid model for the $\text{Ar}^+$ ions and slow electrons

The description of this model is already given in Ref. 11. Here we should only point out that because other ionization collisions were added (see below Sec. II C 1), the production of electrons and  $\text{Ar}^+$  ions was enhanced and consequently, the source terms of the slow electron and  $\text{Ar}^+$  ion continuity equations should include all these processes. The contribution of the  $\text{Cu}^+$  ion density ( $n_{\text{Cu}^+}$ ) to the total charge density was considered and hence explicitly added as a term to the right-hand side of the Poisson equation:

$$\nabla^2 V = -\frac{e}{\epsilon_0}(n_{\text{Ar}^+} + n_{\text{Cu}^+} - n_e - n_{e\text{fast}}), \quad (1)$$

where  $\epsilon_0$  is the permittivity of the free space,  $e$  is the electron charge,  $V$  is the electric potential,  $n_{\text{Ar}^+}$  and  $n_{\text{Cu}^+}$  are the  $\text{Ar}^+$  and  $\text{Cu}^+$  ion densities, respectively, and  $n_e$  and  $n_{e\text{fast}}$  are the slow and fast electron densities, respectively.

### 2. Fluid model for $\text{Ar}^m$ metastable atoms

The transport of  $\text{Ar}^m$  metastable atoms is described by the continuity and flux equations. The production and loss terms of the continuity equation are given by the following processes: radiative recombination of  $\text{Ar}^+$  ions with thermal electrons, and impact excitation by fast electrons, fast  $\text{Ar}^+$  ions, and fast  $\text{Ar}^f$  atoms, were considered as production processes to the metastable state, while the following processes were included as loss mechanisms: fast electron-impact ionization from the metastable state, electron-impact transfer (also called electron quenching) to the resonance level, which decays to the ground state (the resonance levels  $^3P_1$  and  $^1P_1$  have been lumped together into a collective level symbolized by  $\text{Ar}^*$ ), metastable-metastable ionization (also called pooling ionization), Penning ionization of the sputtered Cu atoms, two-body collisions, and three-body collisions with ground-state Ar atoms, and diffusion to the walls

followed by deexcitation at the walls. Electron-impact excitation of metastable atoms to the  $3p^54p$  levels and other high-lying states was not considered as a loss process, because the majority of atoms excited to higher levels radiate down again to the  $3p^54s$  state and hence the net loss of the metastable will be very small. The fast electron, fast  $\text{Ar}^+$  ion, and fast  $\text{Ar}^f$  atom collision rates were calculated in the corresponding Monte Carlo models through the energy-dependent cross sections. The cross section for electron-impact excitation to the metastable state was taken from Mason and Newell,<sup>38</sup> and factorized to the maximum value of the cross section reported (values presented only until 19 eV) by Puech and Torchin,<sup>39</sup> which was recommended by Phelps.<sup>40</sup>

Taking into account the production and loss processes summarized in Table I (Refs. 41–43) and the fact that the flux is only determined by diffusion, the density of the collective metastable state is calculated with the following balance equation:

$$\frac{\partial n_{\text{Ar}^m}}{\partial t} - D_{\text{Ar}^m} \nabla^2 n_{\text{Ar}^m} = S_{\text{prod}} - S_{\text{loss}}, \quad (2)$$

where

$$S_{\text{prod}} = S_{e,\text{exc}} + S_{\text{Ar}^+,\text{exc}} + S_{\text{Ar}^f,\text{exc}} + k_{\text{rec}} n_e n_{\text{Ar}^+},$$

$$S_{\text{loss}} = S_{e,\text{ion},m} + k_{\text{sela}} n_{\text{Ar}^m} n_e + 2k_{\text{pool}} [n_{\text{Ar}^m}]^2 + k_{\text{Pen}} n_{\text{Ar}^m} n_{\text{Cu}} + k_{2B} n_{\text{Ar}^m} n_{\text{Ar}} + k_{3B} n_{\text{Ar}^m} [n_{\text{Ar}}]^2.$$

The boundary conditions are defined based on the fact that a rather high population of metastable atoms was experimentally observed at the cathode walls. Note that in our previous models<sup>11,44</sup> it was assumed that the metastable density at the walls was equal to zero. The processes, which can be responsible for the presence of the metastables at the cathode walls, are most probably (1) recombination of  $\text{Ar}^+$  ions with

electrons at the cathode, yielding the formation of atoms in excited metastable state, (2) when fast  $\text{Ar}^f$  atoms bombard the cathode, a fraction of them might come back to the discharge in the excited metastable state. And (3) a part of the metastable atoms impinging on the cathode surface are not quenched and comes back to the gas phase as metastable atoms. This mechanism has been recently observed with a glass surface.<sup>16</sup> However, quenching probabilities higher than 99% were measured for metal surfaces.<sup>45</sup>

We selected the first possibility because at the concerned energy range, i.e., energies less than 300 eV, the mechanism to induce secondary electron emission by  $\text{Ar}^+$  ions at a clean cathode surface is by potential emission,<sup>46,47</sup> which means neutralization and Auger deexcitation, i.e., the formation of the metastable atoms is implicitly included.

In the present fluid model, the  $\text{Ar}^m$  metastable atom density at the cathode surface was taken equal to the measured  $\text{Ar}^m$  metastable atom density and it is assumed that this population is produced by a fraction of the bombarding  $\text{Ar}^+$  ion flux at the cathode, which after recombination, comes back to the discharge as  $\text{Ar}^m$  metastable atoms. At the anode, the  $\text{Ar}^+$  ion flux is low; most of the discharge current is given by the electron flux.<sup>10</sup> Hence the metastable atom density was taken equal to zero. With these boundary conditions, Eq. (2) is discretized and solved using the extended Thomas algorithm.<sup>48</sup>

### C. Monte Carlo models

The MC simulations can be used to handle situations characterized by strong thermal nonequilibrium,<sup>49</sup> such as for the description of the fast electrons all over the discharge. The particles are followed one after another and the collision rates are calculated based on the energy-dependent cross sections. Hence, an accurate energy distribution function of the particles can be calculated. The dynamics of the particles are determined by Newton's law of motion:  $m_i(d\mathbf{v}/dt) = q_i\mathbf{E}_f$ , where  $m_i$  and  $q_i$  are the mass and the charge of the particle  $i$ , respectively, and  $\mathbf{E}_f$  is the electric field. The velocity of the particles is determined from the integral of motion. The particle position is calculated from the integration of the velocity equation. The average collision probability is reproduced through the energy-dependent collisions cross sections and the generation of random numbers. The self-consistently calculated electric field is obtained from the fluid model for the charged particles, where the continuity and flux equations are solved together with Poisson's equation. (See above: Sec. II B 1.)

In order to calculate more accurately the source terms for the fluid models, the MC approach is applied also to other fast particles, i.e., to the fast  $\text{Cu}^f$  and fast  $\text{Ar}^f$  atoms in the complete discharge, and for the  $\text{Ar}^+$  and  $\text{Cu}^+$  ions in the CDS.

#### 1. Monte Carlo model for the fast electrons

This model was described in Refs. 10 and 11. Here it was extended in order to account for the electron-impact ionization of Cu ground-state atoms. The cross section for this process was taken from Vriens.<sup>50</sup> Beside the cascade elec-

trons, created by electron-impact ionization of the Cu atoms, also the electrons created by Penning ionization were followed.

#### 2. Monte Carlo model for the fast $\text{Ar}^+$ ions and fast $\text{Ar}^f$ atoms

The MC model for  $\text{Ar}^+$  ions and fast  $\text{Ar}^f$  atoms is described in Ref. 11. Here we focus only on the modifications due to the incorporation of the sputtered Cu atoms in the model. Due to asymmetric charge transfer (ACT) of  $\text{Ar}^+$  ions with Cu atoms,  $\text{Ar}^+$  ions are lost. This loss of the  $\text{Ar}^+$  ions is considered in the present MC model through the ACT collision rate calculated in the fluid model for  $\text{Cu}^+$  ions and Cu atoms (see Ref. 33). It should be noted that the loss and creation of charged particles, especially of the  $\text{Ar}^+$  ions and electrons, should always be carefully considered because the  $\text{Ar}^+$  ions, together with the electrons, determine the electrical properties of the glow discharge and they are important in this respect for the current balance. Further, as a result of  $\text{Cu}^+$  ion elastic collisions with the background Ar gas, fast  $\text{Ar}^f$  atoms can be created. These created fast  $\text{Ar}^f$  atoms are fed back to this model and are followed here in the same way as the rest of the fast  $\text{Ar}^f$  atoms. (See Ref. 11 for more details.)

#### D. Coupling of the submodels

The above four submodels, together with the three models for the sputtered species, are coupled to each other due to the interaction processes between the plasma species, and they are solved iteratively until convergence is reached. The latter is determined by the difference in the total current to the anode in two successive iterations, which should be below 1%. Typically, three to four iterations were carried out before convergence was reached.

### III. EXPERIMENTAL SETUP

The HCD geometry consists of a cylindrical hollow cathode copper tube of 1-cm inner diameter and 3-cm length, with a copper-made disk at each tube end. One of those disks acted as anode, while the other disk was connected to the cylindrical hollow cathode (asymmetrical configuration). A narrow slot of 0.1 cm wide and 1 cm long has been machined into each disk in order to allow the map of the laser beam passing through the discharge. This HCD was surrounded by a Pyrex envelope and placed inside a vacuum vessel evacuated by a turbomolecular pump. To eliminate eventual introduction of impurities from outgassing or from microleaks, the vacuum vessel was continuously flushed with 3 SCCM (standard cubic centimeter per minute) of high-purity (99.998%) argon gas. The gas pressure, measured with a capacitance nanometer, was varied from 0.3 to 1 Torr by adjusting the pumping speed with a control valve. The discharge was operated at currents between 0.5 and 10 mA, for which the measured discharge voltage was ranging from 230 to 316 V.

The population of the two metastable states ( $^3P_2$  and  $^3P_0$ ) was measured using optical absorption, with a tunable Littman-type external-cavity diode laser (LD110, Sacher La-

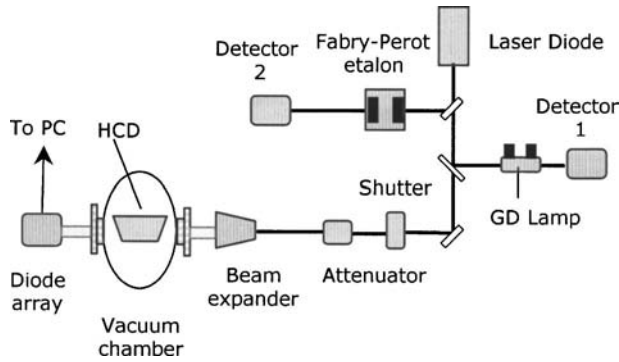


FIG. 1. Schematic overview of the experimental setup.

sertechnik) as light source. The laser was tuned on the transitions  $\lambda=772.42$  and  $772.38$  nm, originating from the  $^3P_2$  and  $^3P_0$  metastable levels, respectively. Figure 1 shows the optical arrangement. Two secondary beams have been obtained using beam splitters. The first beam was used for the precise frequency calibration with a Fabry–Perot interferometer and the absorption signal from the second beam, crossing a low-pressure reference argon glow discharge cell, helped for the exact setting of the laser wavelength at the center of the absorption lines.<sup>15,51</sup> Before entering the vacuum vessel, the main laser beam was attenuated and then horizontally expanded with a set of four-successive grazing angle incidence prisms, which provided a beam map covering the entire surface of the anode slot. Therefore, a  $1.0 \times 0.1$ -cm laser map crossed the HCD cylinder parallel to its axis and exited from the second slot, which was perfectly aligned with the entrance slot. The laser beam was then detected with a photodiode array (PDA-697, Andor Technology), whose 1024 pixels were also aligned with the slots. Hence, each radial position  $r$  in the HDC corresponds to a pixel number,  $n$ . Given the  $25\text{-}\mu\text{m}$  step of the pixels, the laser map covered only 400 pixels of the detector. The PDA was controlled by a personal computer. To record the radial profile of the maximum absorption signal, when the laser wavelength was set at the center of the line, the acquisition of four-files was needed:

- $L_p(n)$ : (plasma and laser on),
- $L_0(n)$ : (laser with plasma off),
- $P(n)$ : (plasma without laser beam, stopped by a shutter), and
- $B(n)$ : (plasma and laser beam off: background, dark counts, and readout noise).

According to the Beer–Lambert law, the radial profile of the metastable atoms density,  $N(r)$ , can be deduced from the following relation:

$$\langle N(r) \rangle = 4\pi\epsilon_0 \frac{mc}{\pi e^2} \frac{\delta\nu_D}{2\sqrt{\ln 2/\pi} lf} \ln \left[ \frac{L_p(n) - P(n)}{L_0(n) - B(n)} \right],$$

where  $m$  and  $e$  are the electrons mass and charge,  $c$  is the light speed,  $\delta\nu_D = (2\sqrt{\ln 2/\lambda_0})/\sqrt{k_B T(t)/M}$  is the Doppler width [full width at half maximum (FWHM)] related to the temperature  $T(r)$  of the metastable atoms,  $l$  is the length of the HCD, and  $f$  is the oscillator strength of the line, whose

values are 0.028 and 0.31 for the 772.38- and 772.42-nm lines, respectively.<sup>52</sup> We estimate a radial resolution better than 0.01 cm, corresponding to 4 pixels. We should point out that the measured populations represent axially averaged values. To avoid saturation phenomena leading to an underestimation of the densities,<sup>53</sup> the intensity of the monitoring laser map was reduced to about  $10 \mu\text{W}/\text{cm}^2$ .

In a preliminary experiment, the laser beam was limited to 0.1 cm in diameter, the PDA was replaced with a photodiode (PD), the laser frequency was modulated (at 10 Hz) around the line center (about 10-GHz modulation), and the signal from the PD, together with the signals from detectors 1 and 2, were recorded with a digital oscilloscope (see for details Refs. 15 and 51). This was done in order to deduce from the Doppler profile of the absorption line the temperature of metastable atoms, which is similar to the gas temperature  $T_g$ , under our pressure conditions.<sup>51</sup> When moving the laser beam along the diameter of the HCD, we did not observe any radial dependence of  $T_g$ , but a slight increase of  $T_g$  with pressure and discharge current was observed. However, to simplify, this dependence of  $T_g$  of the plasma parameters is neglected in the model.

#### IV. RESULTS

The models were applied to a HCD, consisting of a cylindrical cathode closed at one end and a disk anode at the other end, separated by 0.2 cm (see Fig. 1 of Ref. 10). The discharge conditions assumed in the model were taken from the experiment, i.e., the gas pressure was varied from 0.3 to 1.0 Torr, the discharge current ranged from 1 to 9 mA, and a discharge voltage between 249 and 300 V was applied to the cathode, whereas the anode was grounded. The gas temperature was assumed to be at room temperature, 300 K.<sup>54</sup>

##### A. Calculated two-dimensional $\text{Ar}^m$ metastable atom density profiles

Figure 2 shows the calculated two-dimensional Ar metastable density profiles, obtained under the following assumptions, which yielded the best agreement with experiment:

- At the walls, a fraction (in the order of several percent, see Fig. 5) of the  $\text{Ar}^+$ -ion flux comes back as  $\text{Ar}^m$  metastable atoms.
- The electron-quenching rate coefficient is assumed to be equal to  $1 \times 10^{-8} \text{ cm}^3 \text{ s}^{-1}$ .
- It is assumed that the production of  $\text{Ar}^m$  metastable atoms is due to direct electron-impact excitation from the ground state, as well as cascading from higher-lying states, and the electron-impact excitation cross section of Puech and Torchin<sup>39</sup> is adopted.

It is clear from Fig. 2 that, for all the conditions, the  $\text{Ar}^m$  metastable atom density is at maximum near the closed end of the HCD (i.e., at the “cathode bottom”). At 0.3 Torr, the  $\text{Ar}^m$  metastable atom density is more spread out in the entire discharge, due to diffusion, and is characterized by a parabolic shape in the radial direction. With increasing pressure, on the other hand, the  $\text{Ar}^m$  metastable atoms become more

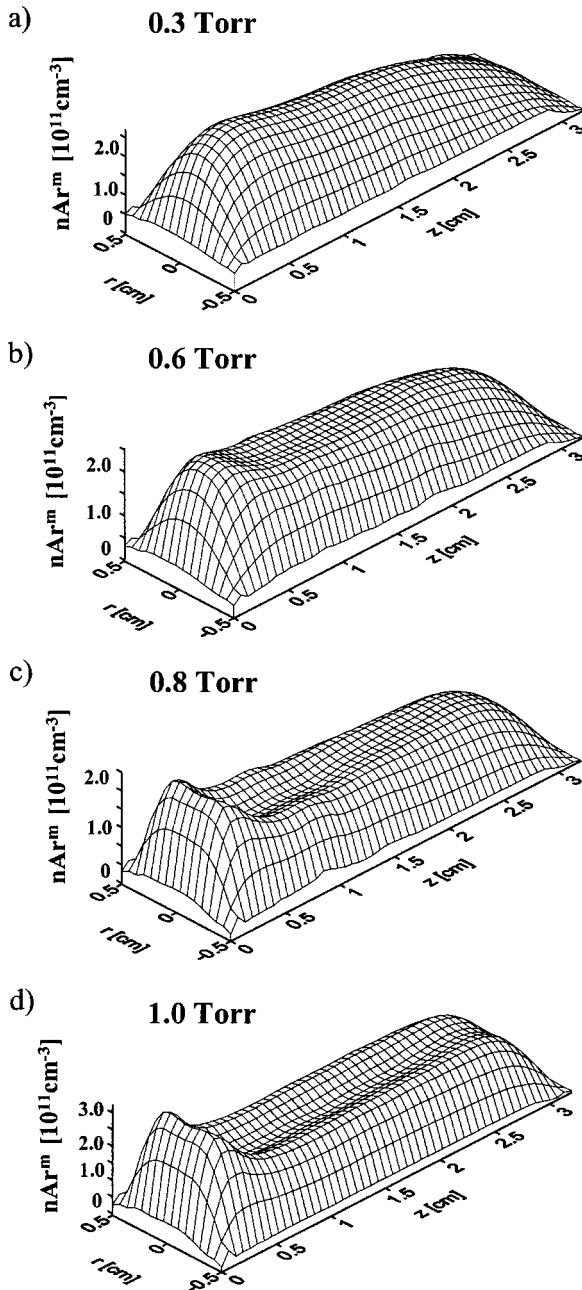


FIG. 2. Calculated two-dimensional profiles of the Ar metastable atom population at 6 mA at 0.3 Torr (a), 0.6 Torr (b), 0.8 Torr (c), and at 1 Torr (d).

concentrated near the cathode bottom, and the metastable density distribution shows a more flat profile in the radial direction, with even the appearance of a dip at the discharge axis.

### B. Comparison between calculated and measured metastable densities

To allow comparison with the measured density profiles (left column of Fig. 3), the calculated two-dimensional Ar<sup>m</sup> metastable density profiles were averaged over the axial distance, and the radial profiles obtained in that way are shown in the right column of Fig. 3. The calculated and measured profiles are in reasonable agreement. At all pressures investigated, the calculated and experimental profiles show a simi-

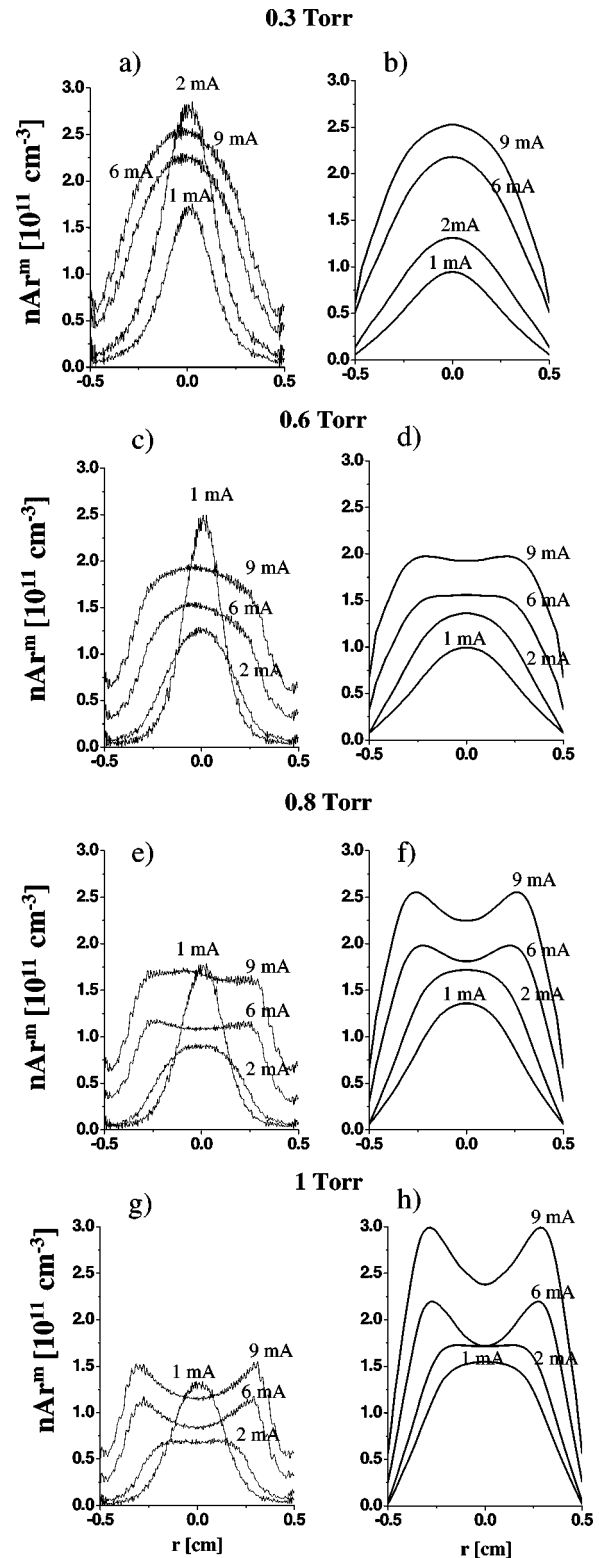


FIG. 3. Radial dependence of the (axially averaged) Ar<sup>m</sup> metastable atom density profiles at four different pressures: experimental profiles (a, c, e, g) and calculated profiles (b, d, f, h).

lar radial dependence as well as variation with current. For instance, at 0.3 Torr, all Ar<sup>m</sup> metastable densities peak at the HCD axis, and show a nearly parabolic profile, which suggests that the loss is dominated by diffusion to the walls and subsequent deexcitation at the walls<sup>55</sup> [Figs. 3(a) and 3(b)]. With increasing pressure, at 0.6 Torr, the profiles begin to

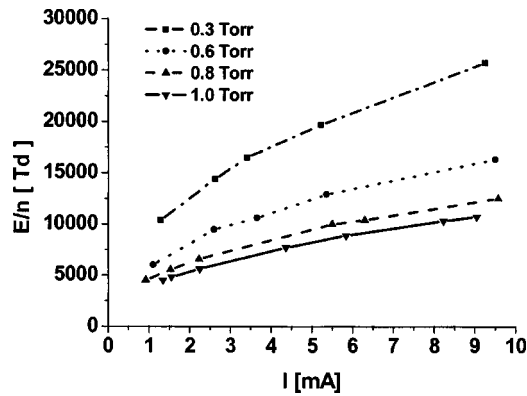


FIG. 4. Calculated (axial average) value of the electric-field strength at the cathode wall, as a function of electrical current, for different values of gas pressure.

flattened at the center (except at 1 mA), which shows that other loss processes are gaining importance [Figs. 3(c) and 3(d)]. With further increase in pressure, at 0.8 Torr, a dip appears at the axis for the profiles corresponding to the high currents [Figs. 3(e) and 3(f)], and finally, at 1 Torr, two maxima in these profiles are clearly observed at the high currents [Figs. 3(g) and 3(h)]. At the current of 1 mA, the densities peak at the center, for all pressures, as in the experiment. One should point out that the calculated density of the metastable atoms at the cathode walls was adjusted to the experimental values by imposing the boundary conditions (see also above: Sec. II B 2).

Indeed, in agreement with our experimental observations, it was assumed in the present model that the metastable population at the cathode walls was not zero. Hence, we assumed that a fraction of the  $\text{Ar}^+$  ions arriving at the cathode, after recombination with the electrons of the conduction band of the metal surface, comes back to the discharge as  $\text{Ar}^m$  metastable atoms. As we can see from Fig. 3, the  $\text{Ar}^m$  metastable density at the walls increases with increasing current (at constant pressure) and with decreasing pressure (at constant current), i.e., at conditions where the reduced electric field increases (see Fig. 4). The increase of the reduced electric field means a rise in the average energy of all charged particles. The fact that the metastable density at the walls increases with the average energy of the impinging  $\text{Ar}^+$  ions may confirm our assumption that the metastable population at the walls is the result of  $\text{Ar}^+$ -ion resonant neutralization at the cathode surface, as the probability of this process increases with rising incoming ion energy.<sup>46</sup>

The percentages of  $\text{Ar}^+$ -ion flux needed to reproduce the metastable density at the walls are shown in Fig. 5, for all the discharge conditions analyzed here. At constant discharge current, this fraction decreases with increasing pressure. This is because at constant current, the ion current to the cathode remains almost constant as the pressure increases, while the diffusion flux of metastable atoms to the wall decreases almost as  $(\text{pressure})^{-1}$ . At constant pressure, this fraction also decreases with increasing current, because the  $\text{Ar}^+$ -ion flux to the cathode increases linearly with the discharge current, while the  $\text{Ar}^m$  metastable flux to the wall changes only slightly. (cf. the curves of 1 and 9 mA in the left column of Fig. 3).

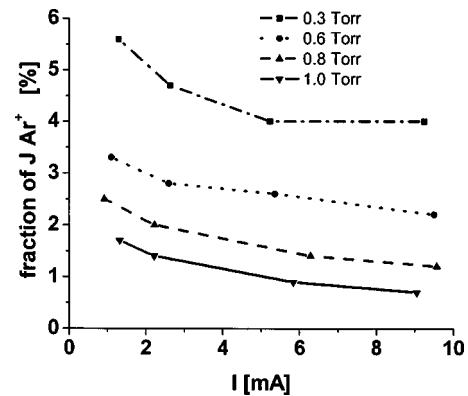


FIG. 5. Calculated fraction (in percent) of the  $\text{Ar}^+$  ion flux at the cathode walls coming back to the discharge as  $\text{Ar}^m$  metastable flux, as a function of the discharge current.

Some features of the measured profiles can, however, not yet correctly be reproduced by the model.

*a. At constant pressure, the calculated  $\text{Ar}^m$  metastable atom densities increase with current, while experimentally this is not the case for the lower currents.* Indeed, the measured metastable population at 1 mA, at its maximum, is higher than the corresponding values for 0.6, 0.8, and 1 Torr, and at 0.3 Torr the maximum metastable density is the highest at 2 mA. The reason for the rise of calculated  $\text{Ar}^m$  metastable atom density with rising current is the increase of total production rate with current, as is shown in Fig. 6. Indeed, the fast electron,  $\text{Ar}^+$  ion, and fast  $\text{Ar}^f$  atom fluxes, which define all production mechanisms, are directly proportional to current. Hence, in order to obtain a drop in calculated  $\text{Ar}^m$  metastable density with rising current, as is observed in the experimental results, the rates of the loss mechanisms should increase more than linearly with current, in order to compensate for the increased production. However, at high current, hence high electron density, the main loss is due to electron quenching (see below, Sec. IV B), for which the rate is only proportional to the current. At low current, hence low electron density, diffusion is the dominant loss mechanism, but it does not depend on current at all. Hence, our model is not able to predict a higher metastable population at low current (e.g., 1 or 2 mA) than at high current (6 or 9 mA).

*b. At constant current, with increasing pressure, the cal-*

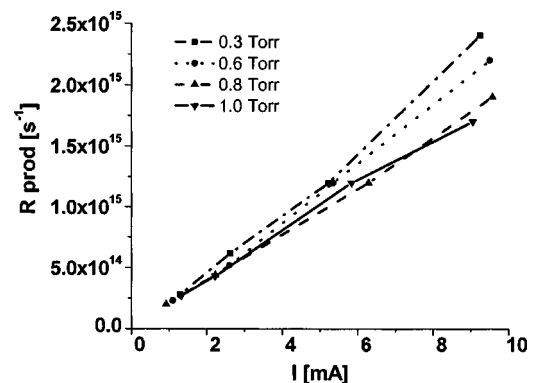


FIG. 6. Total production rate determining the  $\text{Ar}^m$  metastable atom density, integrated over the entire discharge, as a function of total discharge current, at four pressures.

culated metastable density increases, while in the experiment the opposite tendency is observed. As shown in Fig. 6, the total production rate increases slightly with decreasing pressure, although it is worth to mention that the pressure effect is much less pronounced than the current effect, described above. The reason for this increasing production rate with decreasing pressure results from the increasing contribution of fast  $\text{Ar}^+$  ions and  $\text{Ar}^f$  atoms. Indeed, at lower pressures, the reduced electric field increases, as the discharge voltage increases (at constant current), and moreover, the energy relaxation length of  $\text{Ar}^+$  ions inside the CDS rises. So the fast  $\text{Ar}^+$  ions and  $\text{Ar}^f$  atoms have higher energy, and consequently, fast  $\text{Ar}^+$  ion and  $\text{Ar}^f$  atom impact excitation become more efficient as production mechanisms.<sup>11</sup> However, in spite of the increasing production rate with decreasing pressure, the calculated metastable density decreases with decreasing pressure. This is a consequence of the increasing role of diffusion at lower pressure,<sup>13,29,56</sup> spreading out the metastable atoms to the walls, where they are destroyed upon collisions with the wall. At 0.3 Torr, diffusion is the main loss mechanism (see also below, Sec. IV B), as can be deduced from the nearly parabolic shape of the calculated radial profiles.

A similar behavior of increasing  $\text{Ar}^m$  metastable population with increasing pressure and current was also found in an Ar glow discharge with planar cathode in dc (Refs. 18 and 24) and in (Refs. 26 and 57) regimes, where the  $\text{Ar}^m$  metastable population has been measured (by laser-induced fluorescence or by optical emission) and calculated (with a hybrid model) at similar conditions as under study here. Experimental and calculation studies performed in Ar PC discharges<sup>28,29,53</sup> at 0.075–4 Torr show that the metastable population increases up to 0.1 Torr and then decreases, i.e., the metastable population appears to saturate by the effect of pressure at much lower values. This results from the much larger vessel dimensions in these experiments, so that the diffusion rate is significantly reduced, and hence, the relative importance of volume-quenching mechanisms increases.

Hence, although it should be noted that in absolute values, the difference between the calculated and experimental densities is not large [i.e., at maximum a factor of 2, cf. Figs. 3(g) and 3(h)], and can even be considered rather small, in view of the uncertainties in the model (and experiment to a minor degree), we want to investigate in more detail why our model, in its current state, i.e., with the rate coefficients and cross sections used as presented in Table I, predicts a pressure dependence of the metastable atom population, which is opposite to the experimental observations. In the following sections, we will investigate in somewhat more detail the relative contributions of the different production and loss mechanisms, as well as the influence of the rate coefficients and cross sections, in order to find out how a better agreement with experimental data might be obtained.

### C. Production and loss processes determining the metastable density

The effect of the different production and loss mechanisms in modeling the metastable atom density profiles can be understood from Fig. 7, where the radial dependence of

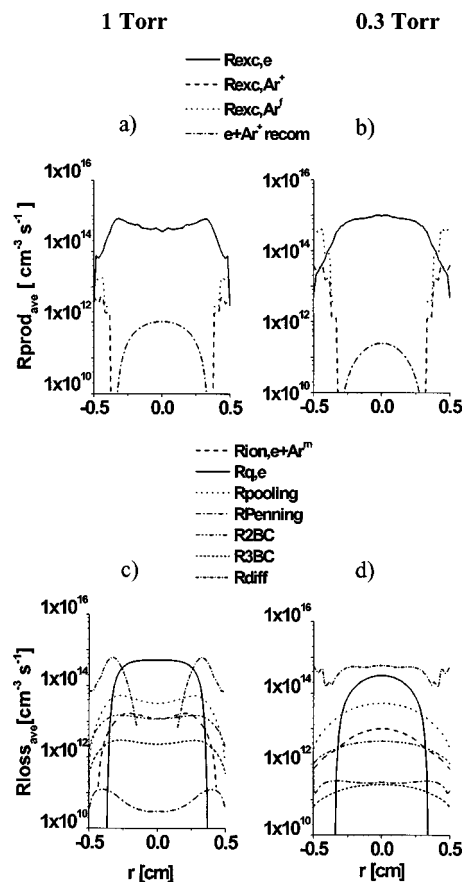


FIG. 7. Calculated radial profiles of the axially averaged production (a,b) and loss (c,d) rates determining the  $\text{Ar}^m$  metastable atom population at 6 mA, at 1 and 0.3 Torr, respectively.

the production and loss rates, averaged over the axial distance, are shown for a discharge of 6 mA, at 1 and 0.3 Torr, as a representative example for all the discharge conditions investigated here.

At 1 Torr, electron-impact excitation ( $R_{\text{exc},e}$ ) is the main production source for the metastable atom population, and the maximum of the electron-impact excitation rate [Fig. 7(a)] is found at the same radial position as the maximum in the metastable density [Figs. 3(g) and 3(h)], i.e., in the NG close to the boundary with the CDS. At this pressure, only a few heavy particles have enough energy for excitation.<sup>11</sup>

With decreasing pressure, as the mean energy of the fast particles increases and taking into account that at energies above 50 eV the cross sections for  $\text{Ar}^+$  ion and  $\text{Ar}^f$  atom impact excitation to the metastable state become higher than the electron-impact excitation cross section, the production rate by heavy particles ( $R_{\text{exc},\text{Ar}^+}$ ,  $R_{\text{exc},\text{Ar}^f}$ ) increases, and they turn out to be the main source for the metastable Ar atoms in the CDS [see Fig. 7(b)]. Electron-impact excitation remains the main production source in the NG and its rate peaks, similar to the metastable profile [Fig. 7(b)], at the center (HCD axis). At low pressures, due to the increase of the reduced electric field and the CDS length (see Figs. 4 and 8), the average electron energy at the discharge axis will be high enough to cause excitation collisions to the metastable state, while at high pressure, very few electrons will reach the discharge axis with sufficient energy to undergo inelastic collisions.

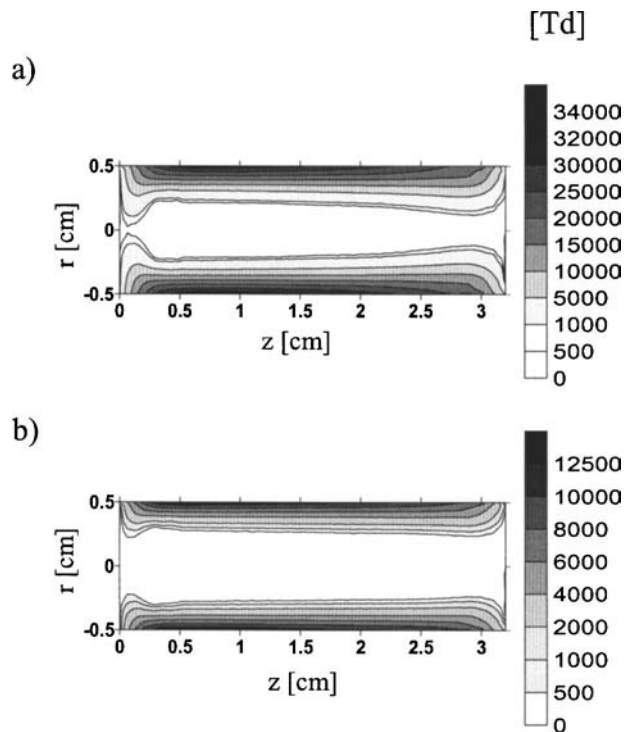


FIG. 8. Calculated radial electric-field distribution throughout the HCD, at 9 mA and at 0.3 Torr (a), and at 1 Torr (b).

The role of electron-ion recombination was found negligible for all the conditions, due to the low ionization degree of the plasma ( $10^{-5}$ – $10^{-4}$ ).<sup>10,11</sup>

Concerning the losses, we see that at 1 Torr the main mechanism of destruction is electron transfer to the resonance level ( $R_{q,e}$ ). Diffusion to the walls becomes important only in the CDS, as the maximum of the metastable atom profile is found in the NG, close to the NG–CDS interface [Fig. 7(c)]. This is in contrast with the calculated results at 0.3 Torr, where diffusion predominates over the other loss processes all over the discharge volume and spreads out the metastable atom population toward the walls, where the metastable atoms undergo deexcitation [Fig. 7(d)].

Figure 9 shows the relative contributions of the different production (a) and loss (b) processes, integrated over the entire discharge, as a function of current, for the different pressures investigated. It is clear from Fig. 9(a) that electron-impact excitation (thin lines) is the dominant production mechanism of Ar metastable atoms, at all conditions investigated, with a contribution ranging from 60% to almost 100%. The contribution decreases slightly with increasing current and decreasing pressure. The reason is that the fast  $\text{Ar}^f$  atoms start to play a quite important role at higher current and lower pressure, as is also observed in Fig. 9(a) (thicker lines). Indeed, a higher current (at constant pressure) and a lower pressure (at constant current) correspond to a higher discharge voltage, hence to a higher reduced electric field (see Fig. 4) and consequently higher energies of the fast  $\text{Ar}^m$  metastable atoms, whereas three-body collisions with Ar gas atoms and Penning ionization of the sputtered Cu atoms were calculated to contribute for less than 1%.

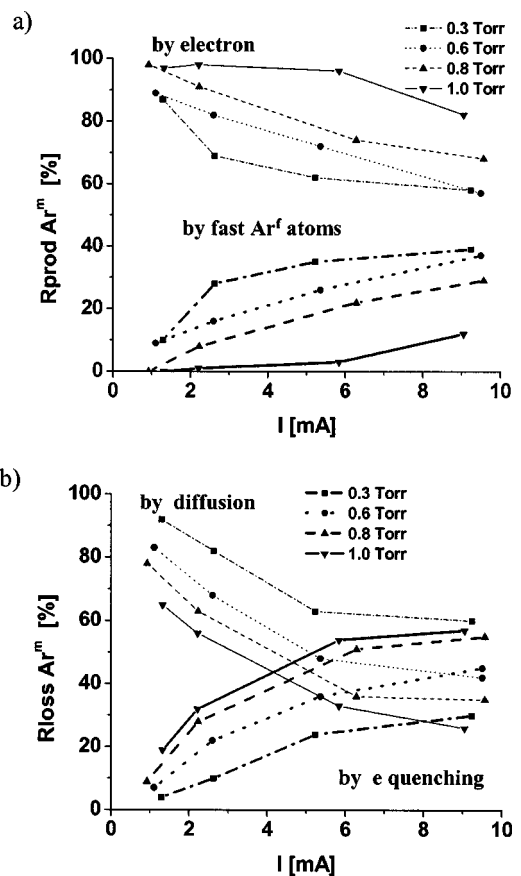


FIG. 9. Calculated relative contributions of the main production (a) and loss (b) processes, integrated over the entire discharge, as a function of current, at four pressures.

increases also slightly with current, and with decreasing pressure, but it was always less than 4%, because of the lower fast  $\text{Ar}^+$ -ion flux and impact excitation cross section compared to the fast  $\text{Ar}^f$  flux<sup>11</sup> and impact excitation cross section.<sup>41</sup> Finally, the contribution of electron-ion recombination is calculated to be negligible as production mechanism of the  $\text{Ar}^m$  metastable atoms, with a typical contribution of less than 0.1%.

Concerning the loss mechanisms [Fig. 9(b)], diffusion to the walls, followed by deexcitation at the walls (thin lines), is calculated to be the dominant loss mechanism at 0.3 Torr and for low currents at all pressures investigated, with contributions ranging from 60% to over 90%. Electron-impact transfer of the metastable to the resonance level (thicker lines) becomes increasingly important at higher current and pressure, and it reaches a contribution of 60% at the highest current and pressure investigated. This is likely expected because of the higher electron densities at higher current and pressure. Some other loss processes (not shown in the figure), such as electron-impact ionization from the metastable level, pooling ionization, and two-body collisions with Ar gas atoms, contribute for a few percent to the total loss of  $\text{Ar}^m$  metastable atoms, whereas three-body collisions with Ar gas atoms and Penning ionization of the sputtered Cu atoms were calculated to contribute for less than 1%.

We can conclude that the Ar metastable atom profiles at pressures of 0.8 and 1 Torr and at currents of 6 and 9 mA are

mainly determined by two factors: (i) enhanced production through electron-impact excitation collision from the ground state, which peaks near the CDS–NG interface, coupled by (ii) enhanced loss, due to thermal electron quenching, at the cylinder axis, i.e., at the position where the maximum of the electron density is found for all the conditions investigated (see, for example, Figs. 6–8 of Ref. 10). With decreasing pressures, the main source of metastable atom production remains the electron-impact excitation from the ground state, but due to the increase of the electron energy relaxation length, the maximum of the electron-impact excitation rate is now shifted to the discharge axis. Moreover, as the discharge pressure drops, the diffusion increases, becoming the main loss, which is reflected by the nearly parabolic radial profile of metastable atom densities at low pressures.

Integrated over the total discharge volume, the ionization due to the metastable atoms was found to be less than 0.5% of the total ionization rate.

#### D. Influence of the electron-quenching rate coefficient

We have found that the profile of the metastable atom population was greatly dependent of the electron-quenching coefficient ( $k_q$ ) employed in the calculations. For example in Ref. 11 we have used a  $k_q=2 \times 10^{-7} \text{ cm}^3 \text{ s}^{-1}$ , which is a value commonly used in models in the literature, when a collective metastable level is assumed,<sup>20,25,30,58</sup> and we obtained for the higher currents (6 and 9 mA), that the dip of the calculated  $\text{Ar}^m$  radial profile at the HCD axis was much more pronounced at 0.8 and 1 Torr. Moreover, at low pressures, the calculated metastable density profiles show also a dip at the HCD axis (see Fig. 8 of Ref. 11) in contrast with the experimental observations.

We assumed in the present work that the effective electron-quenching coefficient for the collective Ar metastable level should be in the same order as the electron-impact transfer coefficient from the metastable  $^3P_2$  level to the radiative level  $^3P_1$ , because these two are the most populated levels of the  $3p^54s$  group. In an Ar afterglow, Sadeghi<sup>59</sup> measured an electron-impact rate coefficient for transfer from the  $^3P_2$  level to the  $^3P_1$  level of  $3.7 \times 10^{-8} \text{ cm}^3 \text{ s}^{-1}$ .

We used an effective quenching coefficient equal to  $1 \times 10^{-8} \text{ cm}^3 \text{ s}^{-1}$  because this yielded calculated density profiles in good agreement with the experimental values (see Fig. 10). We call this an effective electron-quenching coefficient because our model does not consider explicitly all the four  $3p^54s$  levels. Hence, this coefficient implies the total loss of the metastable atoms due to electron-impact transfer from the metastable levels to the radiative levels and also the reverse process. Indeed, radiative levels  $^3P_1$  and  $^1P_1$  are resonant, i.e., due to the imprisonment of resonance radiation, their lifetimes are much higher than their radiative lifetime.<sup>22,56</sup>

Using this value of  $k_q$ , the comparison between the calculated and experimental results shows that the metastable fluid model at 0.3 Torr works well [see Figs. 3(a) and 3(b)], but at higher pressures (0.8 and 1 Torr) it overestimates the metastable atom population [cf. Figs. 3(e)–3(h)]. This can be

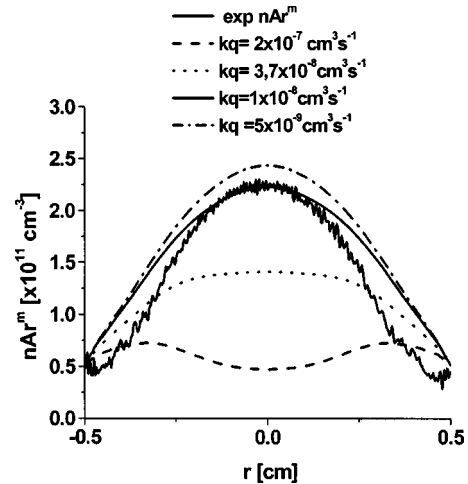


FIG. 10. Effect of considering different values for the electron-quenching coefficients on the calculated  $\text{Ar}^m$  metastable atom density profile, illustrated for a discharge at 0.3 Torr and 6 mA.

a consequence of not considering the interaction between the different excited levels within the  $3p^54s$  state, because at this pressure range, electron quenching was found the main loss process, while at 0.3-Torr diffusion to the walls was found the dominant loss mechanism. Also,  $k_q$  could be electron temperature dependent, hence pressure dependent, a fact that was ignored in our model. However, another reason can be that the total production at higher pressures is overestimated.

#### E. Influence of the electron, fast $\text{Ar}^+$ ion and fast $\text{Ar}^f$ atom impact excitation cross sections

To calculate the rate of electron-impact excitation to the metastable state, which is the main source of production, the integrated electron-impact excitation cross section, also called the optical-excitation cross section, was used for all conditions. This cross section represents the direct excitation from the ground state plus the contributions of excitation to, and subsequent cascading from, higher-lying states. The contribution of the cascading from the higher-lying states in determining the population of the metastable state increases with increasing the reduced electric-field strength.<sup>13,39</sup> At constant current, the reduced electric field increases with decreasing pressure (see Fig. 4), because a constant current at lower pressure arises from a higher discharge voltage. For example, at 9 mA, the reduced electric field, at its maximum value, i.e., at the cathode wall, at 0.3 Torr, is 2.7 times larger than at 1 Torr, as can be seen from Figs. 8(a) and 8(b). Hence it can be deduced that the contribution of cascading from higher states is less important at higher pressure.

At its maximum, the integrated electron-impact excitation cross section to the metastable state presented by Puech and Torchin<sup>39</sup> which includes the contribution of cascading, was equal to  $2.4 \times 10^{-17} \text{ cm}^2$ , which is 2.58 times larger than the maximum of the direct electron-impact excitation cross section<sup>60</sup> (equal to  $9.3 \times 10^{-18} \text{ cm}^2$ ).

Hence, in order to investigate how better agreement can be reached between calculated and measured metastable densities, we have done some additional calculations, assuming that at 1 Torr the metastable atom population is only due to

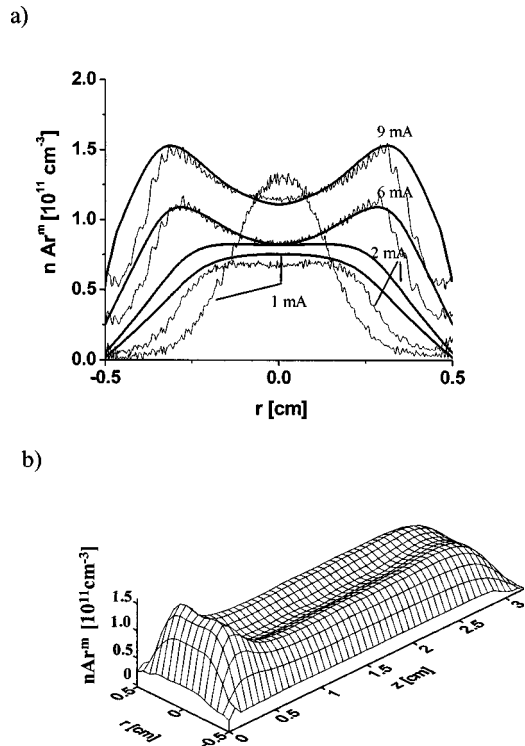


FIG. 11. Comparison of the calculated (axially averaged) and measured  $\text{Ar}^m$  metastable atom density radial profiles at four different currents (a) and the calculated two-dimensional profile of the  $\text{Ar}^m$  metastable atom population at 6 mA (b), after reduction of the total production rate at 1 Torr.

the contribution of direct excitation from the ground state. For this purpose we have reduced the electron excitation cross section of Puech and Torchin by a factor of 2.58. Moreover, we have also reduced by the same factor the  $\text{Ar}^+$  ion and fast  $\text{Ar}^f$  atom impact excitation cross sections to the metastable state, because they were adopted from Phelps,<sup>41</sup> and he considered them as upper limits.

Using these assumptions, the calculated metastable atom populations at 1 Torr have dropped, and averaged over the axial distance, they are in much better agreement with the experimental profiles, as is illustrated in Fig. 11(a). Besides that, the two-dimensional profiles of the  $\text{Ar}^m$  metastable atom density stay (almost) the same [cf. Figs. 11(b) and 2(d)]. The only difference in the profiles is given by the increase of the ratio of the metastable population at the walls compared to its maximum value, as the population at the walls was imposed by the boundary conditions, according to its measured value, and hence it stays the same for these calculations.

#### F. Discrepancy between experiment and model in the CDS

It is, however, apparent from Figs. 3 and 11(a) that for all pressures investigated, the calculated metastable atom population was still found to be higher in the CDS than the experimental values. This can be a consequence of different factors or a combination of them:

- (1) Maybe the  $\text{Ar}^+$  ion and fast Ar atom impact excitation cross sections are too high, which gives an overestimated production in the CDS, or

- (2) it might be that, besides the considered mechanisms, still other loss processes should be included in the model, or
- (3) maybe the rate coefficients of some processes were not accurate enough. For instance, in the CDS, the sputtered Cu atom density, as well as the  $\text{Ar}^m$  metastable density itself, are calculated to be fairly high. Although the overall contribution of Penning ionization (of sputtered Cu atoms) integrated over the entire discharge region is relatively low, this process might play a non-negligible role in the CDS, where the density of the sputtered Cu atoms is quite high. However, the rate coefficient of this process is subject to considerable uncertainty. Indeed, this rate coefficient was only estimated<sup>30</sup> from an empirical formula.<sup>61</sup> Also the rate coefficient of pooling ionization (by collision of two Ar metastable atoms) was taken from Ref. 29, where it was adapted from the corresponding cross section for a similar process in Ne and He. If for these rate coefficients higher values would be adopted, these loss mechanisms might be more important in the CDS, thereby reducing the calculated metastable atom population, so that the latter could be in better agreement with experiment.

However, we do not want to adapt the rate coefficients such as fitting parameters, without any scientific basis, in order to reach better agreement with experiment. We think that more insight can be obtained about the role of different mechanisms, by discussing the discrepancies between model and experiment.

#### V. CONCLUSIONS

We have presented a complete model for an Ar HCD with Cu cathode, and we show the calculation results for the  $\text{Ar}^m$  metastable atoms compared to their experimental density measured by laser absorption. Based on experimental results, the following assumptions were made in the model:

- (1) A fraction (in the order of several percent) of the  $\text{Ar}^+$ -ion flux at the cathode walls returns back to the discharge as  $\text{Ar}^m$  metastable atoms;
- (2) The value for the electron-quenching rate coefficient is assumed to be equal to  $1 \times 10^{-8} \text{ cm}^3 \text{ s}^{-1}$ , which is reasonable, compared to the measured values.

It was found that at low pressure, the metastable atom densities show a nearly parabolic profile at all currents investigated because of the important role of diffusion. When the pressure increases, the density profiles become flatter, and at high currents, they even exhibit two peaks at the CDS–NG boundaries, with a dip at the discharge axis, which is determined mainly by the enhanced production by electron-impact excitation close to the CDS–NG boundaries and the increasing role of the electron quenching as a loss mechanism of the metastable atom population.

The contribution of metastable atoms to the formation of charges in the discharge is found to be negligible for the conditions under study, both as ionization source as well as in secondary electron emission from the cathode.

Finally, from the comparison between calculations and

experiment, we could obtain a better insight in the relative importance of different production and loss mechanisms, and their corresponding rate coefficients and cross sections. The metastable atom densities, calculated in this way, can be used in our model, to predict their importance in the HCD, for instance for Penning ionization of sputtered Cu atoms.<sup>33</sup>

## ACKNOWLEDGMENTS

Two of the authors (N.B. and A.B.) are indebted to the Flemish Fund for Scientific Research (FWO) for financial support. This research is sponsored by NATO's Scientific Affairs Division in the framework of the Science for Peace Programme, by the FWO research project G.0043.01 and by the Federal Services for Scientific, Cultural and Technical Affairs of the Prime Minister's Office through IUAP V. One of the authors (Z.D.) acknowledges partial support from the Hungarian Fund for Scientific Research (OTKA-T-34156), the hospitality of the Laboratoire de Spectrometrie Physique Grenoble, and the financial support of the experimental work from the University of Antwerp.

- <sup>1</sup>A. Goldamn and J. Amoroux, *Macroscopic Process and Discharges* (Plenum, New York, 1983).  
<sup>2</sup>K. Rozsa, *Z. Naturforsch. A* **35**, 649 (1980).  
<sup>3</sup>I. G. Ivanov, E. L. Latush, and M. F. Sem, *Metal Vapour Ions Lasers: Kinetic Processes and Gas Discharges* (Wiley, England, 1996).  
<sup>4</sup>N. K. Vuchkov, K. A. Temelkov, and N. V. Sabotinov, *IEEE J. Quantum Electron.* **35**, 1799 (1999).  
<sup>5</sup>E. M. Oks, A. V. Vizir, and G. Y. Yushkov, *Rev. Sci. Instrum.* **69**, 853 (1998).  
<sup>6</sup>P. J. Slevin and W. W. Harrison, *Appl. Spectrosc. Rev.* **10**, 201 (1975).  
<sup>7</sup>S. Caroli, *Prog. Anal. At. Spectrosc.* **6**, 253 (1983).  
<sup>8</sup>K. Gilmodinov, B. Radziuk, M. Sperling, B. Welz, and K. Nagulin, *Appl. Spectrosc.* **49**, 413 (1995).  
<sup>9</sup>C. Schepers and J. A. C. Broekaert, *J. Anal. At. Spectrom.* **15**, 61 (2000).  
<sup>10</sup>N. Baguer, A. Bogaerts, and R. Gijbels, *Spectrochim. Acta, Part B* **57**, 311 (2002).  
<sup>11</sup>N. Baguer, A. Bogaerts, and R. Gijbels, *J. Appl. Phys.* **94**, 2212 (2003).  
<sup>12</sup>E. Ebbinghaus, *Ann. Phys.* **7**, 267 (1930).  
<sup>13</sup>K. Tachibana, *Phys. Rev. A* **34**, 1007 (1986).  
<sup>14</sup>K. E. Greenberg and G. A. Hebner, *J. Appl. Phys.* **73**, 8126 (1993).  
<sup>15</sup>B. Clarenbach, B. Lorenz, M. Krämer, and N. Sadeghi, *Plasma Sources Sci. Technol.* **12**, 345 (2003).  
<sup>16</sup>P. Macko and N. Sadeghi, *Plasma Sources Sci. Technol.* **13**, 303 (2004).  
<sup>17</sup>G. R. Scheller, R. Gottsho, B. D. Graves, and T. Itrator, *J. Appl. Phys.* **64**, 598 (1988).  
<sup>18</sup>B. K. McMillan and M. Zachariah, *J. Appl. Phys.* **77**, 5538 (1995).  
<sup>19</sup>J. Vlcek, *J. Phys. D* **22**, 623 (1989).  
<sup>20</sup>D. P. Lymberopoulos and D. J. Economou, *J. Appl. Phys.* **73**, 3668 (1993).

- <sup>21</sup>P. A. Sa, J. Loureiro, and C. M. Ferreira, *J. Phys. D* **27**, 1171 (1994).  
<sup>22</sup>E. Ellis and N. D. Twiddy, *J. Phys. B* **2**, 1366 (1969).  
<sup>23</sup>A. V. Phelps and J. P. Molnar, *Phys. Rev.* **89**, 1202 (1952).  
<sup>24</sup>A. Bogaerts, R. D. Guenard, B. W. Smith, J. D. Winefordner, W. W. Harrison, and R. Gijbels, *Spectrochim. Acta, Part B* **52**, 219 (1997).  
<sup>25</sup>T. Makabe, N. Nakano, and Y. Yamaguchi, *Phys. Rev. A* **45**, 2520 (1992).  
<sup>26</sup>S. Rauf and M. J. Kushner, *J. Appl. Phys.* **82**, 2805 (1997).  
<sup>27</sup>G. A. Hebner and P. A. Miller, *J. Appl. Phys.* **87**, 8304 (2000).  
<sup>28</sup>K. A. Hardy and W. Sheldon, *J. Appl. Phys.* **53**, 8532 (1982).  
<sup>29</sup>C. M. Ferreira, L. Loureiro, and A. Ricard, *J. Appl. Phys.* **54**, 2261 (1983).  
<sup>30</sup>A. Bogaerts and R. Gijbels, *Phys. Rev. A* **52**, 3743 (1995).  
<sup>31</sup>M. Surendra, D. B. Graves, and G. M. Jellum, *Phys. Rev. A* **41**, 1112 (1990).  
<sup>32</sup>N. Sadeghi, M. Cheaib, and D. W. Setser, *J. Chem. Phys.* **90**, 219 (1989).  
<sup>33</sup>N. Baguer and A. Bogaerts, *J. Appl. Phys.* (submitted).  
<sup>34</sup>A. Bogaerts and R. Gijbels, *J. Appl. Phys.* **79**, 1279 (1996).  
<sup>35</sup>A. Bogaerts, A. Okhrimovskyy, N. Baguer, and R. Gijbels, *Plasma Sources Sci. Technol.* **14**, 191 (2005).  
<sup>36</sup>T. J. M. Boyd and J. J. Sanderson, *Plasma Dynamics* (Nelson, London, 1969).  
<sup>37</sup>I. P. Shkarofsky, T. W. Johnston, and M. P. Bachiynski, *The Particle Kinetic of the Plasma* (Addison-Wesley, Reading, MA, 1966).  
<sup>38</sup>N. J. Mason and W. R. Newell, *J. Phys. B* **20**, 1357 (1987).  
<sup>39</sup>V. Puech and L. Torchin, *J. Phys. D* **19**, 2309 (1986).  
<sup>40</sup>A. Phelps, [www.colorado.edu/www/research/colldata.html](http://www.colorado.edu/www/research/colldata.html)  
<sup>41</sup>A. V. Phelps, *J. Phys. Chem. Ref. Data* **20**, 557 (1991).  
<sup>42</sup>M. A. Biondi, *Phys. Rev.* **129**, 1181 (1963).  
<sup>43</sup>H. A. Hyman, *Phys. Rev. A* **20**, 855 (1979).  
<sup>44</sup>N. Baguer, A. Bogaerts, and R. Gijbels, *J. Appl. Phys.* **93**, 47 (2003).  
<sup>45</sup>H. Conrad, G. Ertl, J. Küppers, W. Sesselmann, B. Woratschek, and H. Haberland, *Surf. Sci.* **117**, 98 (1982).  
<sup>46</sup>H. D. Hagstrum, *Phys. Rev.* **96**, 336 (1954).  
<sup>47</sup>G. Hohler, *Particle Induced Electron Emission II* (Springer, Berlin, 1992).  
<sup>48</sup>D. U. Rosenberg, *Methods for the Numerical Solutions of Partial Differential Equations* (Elsevier, New York, 1969).  
<sup>49</sup>F. W. Hockney and J. W. Eastwood, *Computer Simulation using Particles* (Adam Hilger, Bristol, 1988).  
<sup>50</sup>L. Vriens, *Phys. Lett.* **8**, 260 (1964).  
<sup>51</sup>R. Engeln, S. Mazouffre, P. Vankan, D. C. Schram, and N. Sadeghi, *Plasma Sources Sci. Technol.* **10**, 595 (2001).  
<sup>52</sup>W. L. Wiese, J. W. Brault, K. Danzmann, V. Helbig, and M. Kock, *Phys. Rev. A* **39**, 2461 (1989).  
<sup>53</sup>N. Sadeghi, *J. Plasma Fusion Res.* **80**, 767 (2004).  
<sup>54</sup>G. H. Copley and C. S. Lee, *Can. J. Phys.* **53**, 1705 (1975).  
<sup>55</sup>A. von Engel, *Ionized Gases* (Clarendon, Oxford, 1955).  
<sup>56</sup>A. Phelps, *Phys. Rev.* **114**, 1011 (1959).  
<sup>57</sup>F. Tochikubo, Z. L. Petrovic, and S. Kakuta, *Jpn. J. Appl. Phys., Part 1* **33**, 4271 (1994).  
<sup>58</sup>E. V. Karoulina and Yu A. Lebedev, *J. Phys. D* **25**, 401 (1992).  
<sup>59</sup>N. Sadeghi, Ph.D. thesis, Grenoble (1974).  
<sup>60</sup>N. T. Padial, G. D. Meneses, F. J. Paixao, and Gy. Csanak, *Phys. Rev. A* **23**, 2194 (1980).  
<sup>61</sup>L. A. Riseberg, W. F. Parks, and L. D. Schearer, *Phys. Rev. A* **8**, 1962 (1973).